FI SEVIER

Contents lists available at ScienceDirect

Materials Characterization

journal homepage: www.elsevier.com/locate/matchar



Synthesis of cobalt-oxide nanoparticles embedded in silicon nanotubes via low-energy cobalt implantation

Roberto Gonzalez-Rodriguez^a, *, Bibhudutta Rout^a, Satyabrata Singh^a, Diana Berman^b, Evan Hathaway^a, Jeffery L. Coffer^c, Yuankun Lin^a, Jingbiao Cui^a

- ^a Department of Physics, University of North Texas, Denton, TX, USA
- ^b Department of Materials Science and Engineering, University of North Texas, Denton, TX, USA
- c Department of Chemistry and Biochemistry, Texas Christian University, TCU Box 298860, Fort Worth, TX 76129, USA.

ARTICLE INFO

Keywords: Silicon nanotubes Ion implantation Cobalt oxide

ABSTRACT

Silicon nanotubes (Si NTs) show a unique structure compared to other silicon nanostructures, such as porous silicon, silicon nanoparticles, and silicon nanowires. Si NTs' well-defined structure in terms of silicon shell thickness, inner diameter, and length with a high surface area makes them useful in myriad applications. In this work, we fabricate Si NTs by using ZnO nanowires as templates; the Si NTs have a shell thickness of ~13 nm, inner diameter of ~80 nm, and a length in the range of $1-2~\mu m$ with embedded Co_3O_4 nanoparticles (NPs), which are formed by annealing the cobalt ion-implanted Si NTs. The cobalt ion implantation was carried out at 50 keV with a fluence of $7.5~\times~10^{15}~ions/cm^2$. The morphology and composition of the cobalt-NP decorated Si NTs are characterized by using scanning electron microscopy (SEM), energy dispersive x-ray spectroscopy (EDX), transmission electron microscopy (TEM), and x-ray photoemission spectroscopy (XPS). TEM, HRTEM, XPS, and Raman spectroscopy studies confirm the formation of Co_3O_4 nanoparticles in the NTs. The temperature-dependent zero-field-cooled (ZFC), and field-cooled (FC) magnetization for the Co implanted Si NTs before and after annealing is also measured and shows little magnetic response due to the low concentration of cobalt in the nanotubes. The fabrication process is compatible with the current semiconductor industry methods and may find potential applications in magnetic drug delivery and devices.

1. Introduction

Nanostructured silicon has multiple applications in lithium-ion batteries, photovoltaics, drug delivery, gene delivery, bioimaging, magnetic resonance imaging (MRI), and electronics [1–5]. One such silicon nanostructure is silicon nanostructures such as porous silicon (pSi) because of their well-defined structure, namely their length, shell thickness, and inner diameter. In contrast, the pSi has a dendritic structure where the porous are interconnected [6,7]. Si NTs can be produced using a number of different methods, including arch discharge, alumina template, and ZnO nanowire template [8]. of these methods, using ZnO nanowires as a template is one of the best ways to grow Si NTs because of its ability to accurately control the inner diameter, length, and shell thickness of the nanotubes. The inner diameter and length of the Si NTs can be tuned by changing the dimensions of the ZnO nanowire templates with the ZnO nanowire's length and diameter. At the same time,

the shell thickness is controlled by the deposition parameters of the silicon layers grown on top of the ZnO nanowires. After the deposition of silicon onto the ZnO nanowires, the wires are etched away using a 1% HCl solution, leaving behind the desired Si NTs. As for the arch discharge method, it simultaneously produces a mixture of silicon nanoparticles, nanowires, and nanotubes, with meager yields of Si NTs due to the majority of the products being nanoparticles [8,9], and it is difficult to separate Si NTs from the other products by the arc discharge method. Using alumina oxide as a template method can easily overfill the pore size, producing silicon wires rather than Si NTs [10]. For these reasons, we use the ZnO nanowires as a template to fabricate Si NTs with controllable sizes.

Cobalt is a d-block transition metal with unique properties useful for catalysts, nanosensors, and nanoelectronics applications [11,12]. Several methods have been used to produce cobalt nanostructures, including hydrothermal processing, electrodeposition, pyrolysis, and polyol. However, these methods are incompatible with current microelectronic

E-mail address: roberto.gonzalezrodriguez@unt.edu (R. Gonzalez-Rodriguez).

https://doi.org/10.1016/j.matchar.2024.113850

Received 8 December 2023; Received in revised form 11 March 2024; Accepted 20 March 2024 1044-5803/© 20XX

Corresponding author.

industry standards, among other issues such as precise control of the particle size and agglomeration [13]. [14–16] When the cobalt is oxidized as Co_3O_4 , it presents different states, making it very attractive for spintronics applications. This is because Co_3O_4 has a transition from ferromagnetic to antiferromagnetic at Neel temperature ~ 30 K. This temperature is increased when pressure is applied due to a change from normal spinel to inverse spinel [17,18]. However, these applications have yet to be exploited due to the complexity of the magnetic structure. [17,19,20] Therefore, the incorporation of Co_3O_4 nanoparticles (NPs) into Si NTs may have potential applications in nanoelectronics and spintronics while being compatible with the current industry standard silicon processing technologies.

In this work, cobalt nanostructures were fabricated inside Si NTs via implantation of low-energy cobalt ions and post-thermal annealing. The Si NTs were fabricated using ZnO nanowires as templates, with Si NTs dimensions of inner diameter ~ 80 nm, shell thickness ~ 13 nm, and length in the 1–2 μm range. To our knowledge, the cobalt-decorated Si NTs via ion implantation have not been reported before. Ion implantation is generally used to introduce targeted dopants into various substrates in a very controlled way. The concentration and desired depth of the doping or impurity elements can be controlled by changing the ion fluence and ion energy during the implantation process. In this case, we used a fluence of 7.5×10^{15} ions/cm² using a low energy ion implantation at 50 keV. The depth and concentration profiles of the ions in the substrate mainly depend on the mass, energy, fluence, and angle of incidence of the implanted ions. The energy of the incident ions can be tuned depending on the required depth profile of the implanted ions [21]. After an annealing process, we observed the formation of Co₃O₄ NPs on the Si NTs. The structure and properties of the Si NTs decorated with cobalt ions were studied by Scanning electron microscopy (SEM), Transmission Electron microscopy (TEM), Raman, and X-ray photoelectron spectroscopy (XPS). Our approach using ion implantation for Si NT decoration with cobalt oxide provides an easy way to control the concentration of the nanoparticles. It can be generalized to other metal ele-

2. Results and discussion

As discussed in our previous work, we used ZnO nanowires as a sacrificial template for fabricating Si NTs, where different diameters, lengths, and shell thicknesses for these Si NTs were reported [22–24]. A diagram of the fabrication process is shown in Fig. S1. First, ZnO nanocrystal seeds were synthesized using hydrothermal and deposited on the substrate using the spin coating method, followed by annealing at 300 °C. A typical (TEM) image of these ZnO nanocrystals is shown in Fig. S2. The ZnO seeds have diameters ranging from 1 to 5 nm and are highly crystalline with a lattice spacing of d = 0.276 nm corresponding to the (100) plane of ZnO. The inset of Fig. S2 is the Fast Fourier Transform (FFT) of the TEM image and demonstrates the polycrystalline structure of the ZnO nanocrystals with random crystal orientations. The ZnO nanowires were grown by a hydrothermal process on the substrate coated with the ZnO seeds. Fig. S3 shows a typical SEM image of these ZnO nanowires. Note that the diameter of the ZnO nanowires determines the Si NTs' inner diameter and length. The silicon shell was deposited onto the ZnO nanowires using a chemical vapor process, and the Si deposition conditions and time controlled the shell thickness. After etching the ZnO core away, the Si NTs were formed, as shown in Figs. 1a and 1b. Fig. 1c shows the distribution of the Si NT wall thickness with an average value of 13. 2 \pm 2.4 nm. Fig. 1a-b shows typical TEM images of the Si NTs after etching, while the corresponding SEM images are shown in Fig. S4.

In this study, we selected the deposition condition to produce Si NTs with inner diameters of ~ 80 nm, tube wall thicknesses of ~ 13 nm, and lengths in the range of 1-2 µm. After the cobalt ion implantation, the Si NTs were annealed in a helium atmosphere to form Co_3O_4 NPs. Fig.

S4a-b shows the Si NTs before and after the Co ion implantation, while Fig. S4c shows an image after the annealing in helium gas at 600 °C for 2 h. The SEM images show that the morphology of Si NTs is unaffected by the ion implantation and annealing processes. Figs. 1d-e and 1 g-h show TEM images of Si NTs after the ion implantation and annealing processes. A deformation in the tips of the Si NTs is observed due to the ion implantation. The tube wall thickness increased from 13.2 ± 2.4 nm to 19.4 ± 3.8 nm, as shown by the size distribution in Fig. 1c and 1f and Fig. S5. This volume swelling in the Co implanted Si NTs can be attributed to the formation of nanovoids/vacancy clusters and nano-bubbles in the tube wall [25,26]. The Co implantation process causes the deformation of the NTs in the tip due to a tilt of NTs of about 20 degrees with respect to the flux of the ion source. Note that Co₃O₄ NPs are not observed before annealing. Therefore, the annealing process is necessary to form the Co₃O₄ NPs with an average size of 3.3 ± 1.3 nm, as shown in Fig. 1i. The formation of Co_3O_4 NPs is most likely attributed to an Ostwald-type ripening process. In this process, the initial step is the cobalt ion implantation in the Si NTs; during this step, depending on the ion implantation fluence, the substrate can suffer damage, which can be reversible or irreversible. In this case, with the fluence of 7.5×1015 ions/cm2, the Si NTs suffer damage due to the formation of the vacancy clusters, nanovoids, and nanobubble created within the Si NTs. With the thermal annealing at 600 °C, the ion's mobility produces a local saturation followed by nucleation with the growth of the Co₃O₄ NPs, and the final step is coalescence [27,28]. In future experiments, Co₃O₄ NPs can be controlled with ion implantation conditions such as fluence, time, vacuum pressure, the energy of the implanted ions, and substrate conditions such as temperature and nanotube dimensions.

Fig. 2 shows the TEM-EDX maps of the Co implanted Si NTs after annealing. A uniform distribution of Co is observed with an atomic percentage value of 1.03% Co in the Si NTs. High-resolution TEM (HRTEM) images of the as-prepared Co implanted Si NTs before and after annealing are shown in Fig. 3a-d. The corresponding FFTs are also included in the inset. The fresh Si NTs have a lattice spacing d = 0.310 nm associated with the silicon (111) plane (Fig. 3a). This proves the Si NTs are polycrystalline after the fabrication process, as shown on the FFT [29]. After the ion implantation, the Si NTs are no longer crystalline, as shown in Fig. 3b and corroborated by the FFT in the inset. It suggests that the Co ion implantation destroys the crystalline structure of Si due to the creation of defects such as vacancies and nanovoids within the Si NTs' structure. After annealing, Co₃O₄ NPs are formed within Si NTs (Fig. 3 c-d). The particles are found to have lattice spacing d = 0.188 nm and d = 0.209 nm, which correspond to the (101) and (100) planes of cobalt oxide, respectively [30]. One can also see that the crystallinity of Si with lattice spacing d = 0.310 nm is restored after annealing, as shown in Fig. 3c.

Fig. 4 shows Raman spectra taken on the as-prepared Si NTs and those of Co implanted Si NTs before and after the annealing process. The as-prepared Si NTs have a Raman mode at 496 cm⁻¹, consistent with nanocrystalline silicon. However, only a weak and broad Raman peak around 480 cm⁻¹ from amorphous Si is observed after Co ion implantation. This is consistent with our previous observations from HRTEM (Fig. 3a-b), which show the destruction of the crystalline structure of the Si NTs after implantation. After the annealing process, a strong Si Raman peak at 500 cm⁻¹ is observed, again demonstrating the recovery of the crystalline Si domain in the Si NTs, consistent with HRTEM measurements. In addition, two other broad peaks at $\sim\!300~\text{cm}^{-1}$ and $\sim 970~\text{cm}^{-1}$ are observed in both the as-prepared and annealed Si NTs, which are consistent with the scattering of two transverse acoustic (2TA) phonons and two transverse optical (2TO) phonons respectively for silicon.

X-ray photoelectron spectroscopy (XPS) was performed on the Co implanted Si NTs before and after annealing, as shown in Fig. 5. A Co 2p signal is observed in both samples with and without annealing. Before

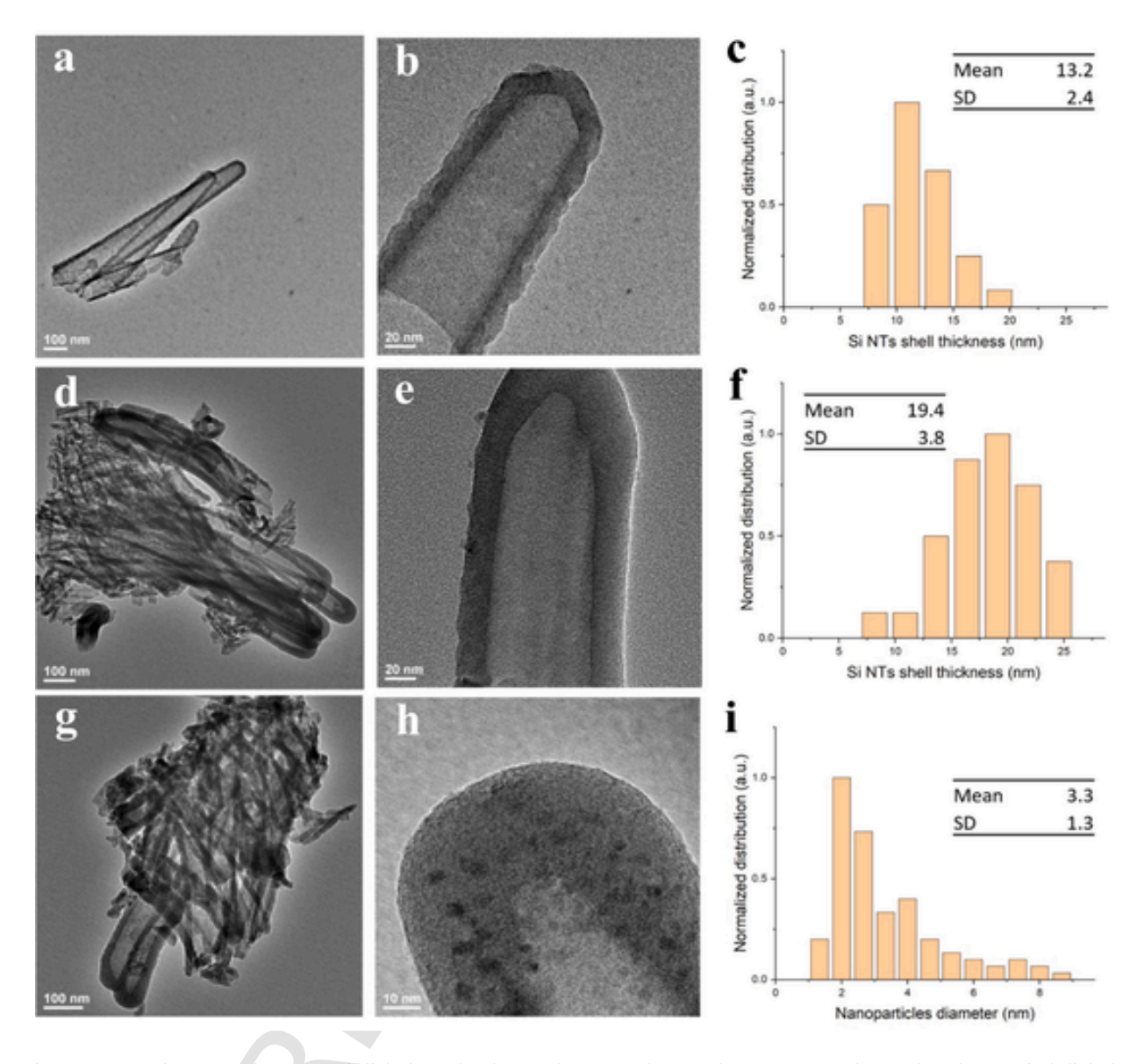


Fig. 1. a-b) TEM images of as-prepared Si NTs; c) Shell thickness distribution of as-prepared Si NTs; d-e) TEM images of Co implanted Si NTs; f) Shell thickness size distribution after Co implantation; g-h) TEM images of Co implanted Si NTs after annealing; and i) Size distribution of Co₃O₄ NPs.

annealing, Co³⁺ at 780.05 eV (Co 2p3/2) and Co²⁺ at 781.7 eV (Co 2p3/2) are observed in the XPS spectra; these values are consistent with the reported in the literature for Co₃O₄, which the sample contains 15.5% Co³⁺ and 84.5% Co²⁺ respectively [31–33]. After annealing, it emerges in the spectrum with 53.2%, 46.8% of Co³⁺, and Co²⁺, respectively. This confirms the presence of the Co₃O₄ NP compositions.

Temperature-dependent zero-field-cooled (ZFC) and field-cooled (FC) magnetization for the Co implanted Si NTs before and after annealing are given in Fig. 6a. No significant difference is detected between the samples before and after annealing. A VSM plot measured at 300 K and 5 K is shown in Fig. 6b-c. Both samples show a linear response in the magnetization without a hysteresis loop at both 5 and 300 K. For this reason, the remanence and the coercivity values have not been calculated. This poor magnetic response is likely due to the extremely small amount of Co contained in the sample. The Si NTs samples have silicon in the micrograms range, with the amount of cobalt having only a 1% atomic concentration. Therefore, it is not surprising that no significant magnetic response was observed.

3. Conclusions

In conclusion, we have fabricated Si NT arrays using a ZnO template process and decorated the NTs with Co via a targeted energy ion implantation process. The Si NTs dimensions were ~ 13 nm shell thickness, $\sim\!80$ nm inner diameter, and $1\text{--}2~\mu\text{m}$ length. The ion implantation was done with a fluence of $7.5\times10^{15}~\text{ions/cm}^2$ using a low-energy ion implantation at 50 KeV. The structural and compositional studies utilizing TEM, HRTEM, XPS, and Raman spectroscopy confirm the formation of Co $_3$ O $_4$ nanoparticles in the NTs. This material composition opens the possibility for magnetics device applications through a process compatible with the current semiconductor industry.

4. Experimental methods

4.1. Materials and equipment

From Sigma-Aldrich were purchased: Zinc acetate Zn(CH₃COO)₂·2H₂O, sodium hydroxide NaOH, methanol MeOH,

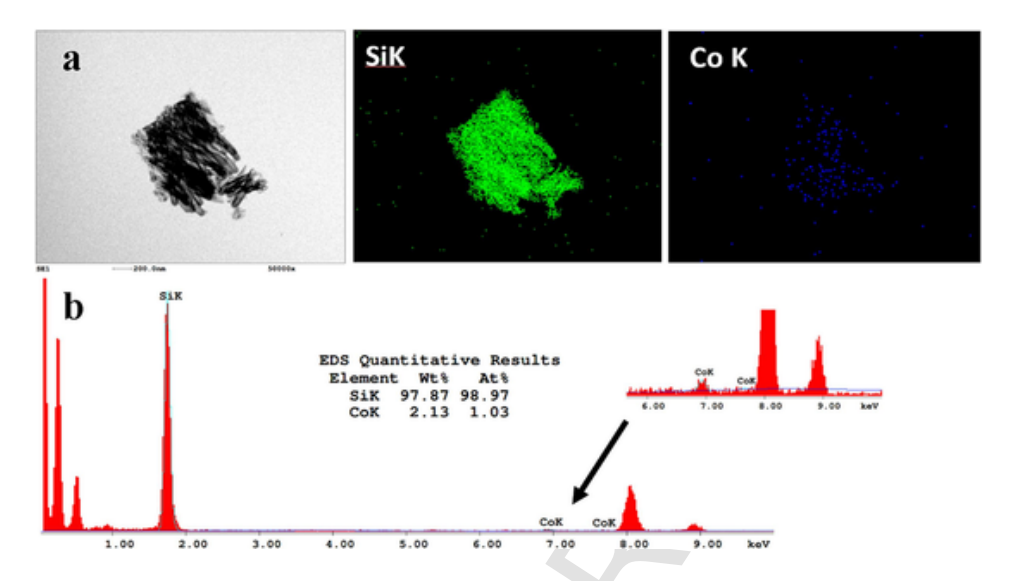


Fig. 2. (a) TEM-EDX maps and (b) typical EDX spectrum of the Co-implanted Si NTs.

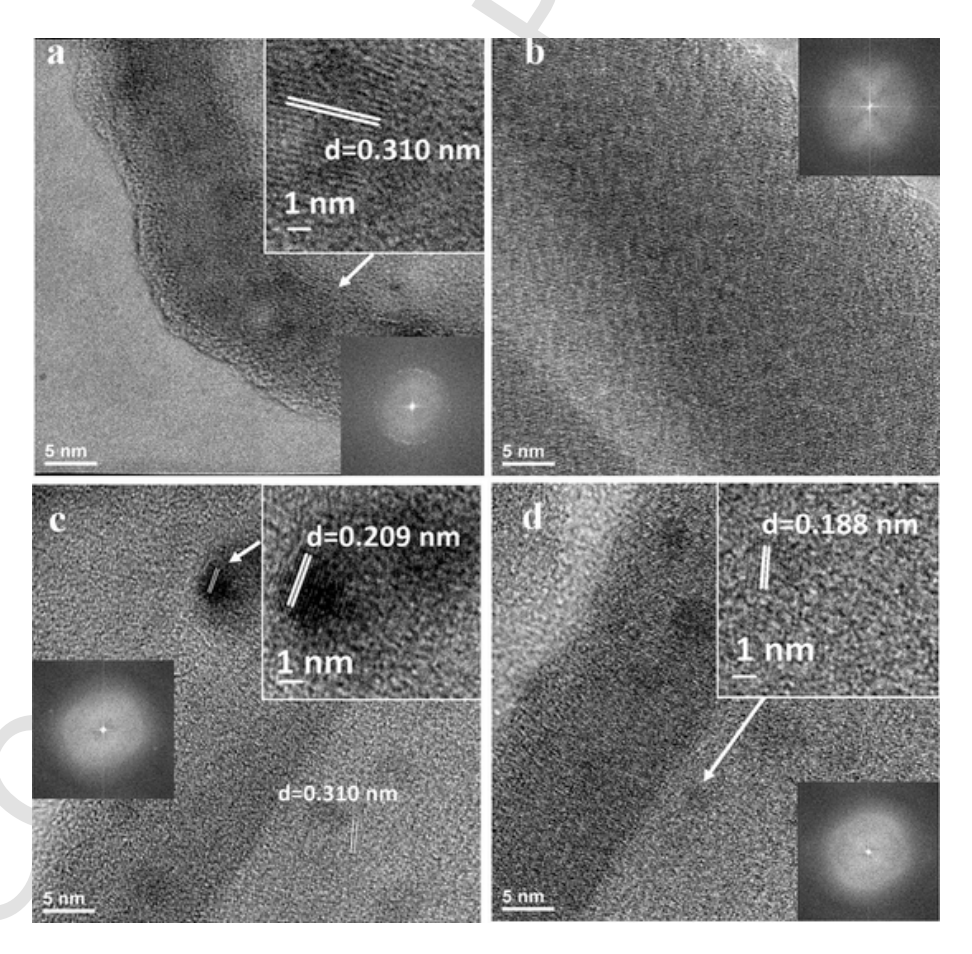


Fig. 3. HRTEM of a) Si NTs, b) Co implanted in Si NTs, and c-d) Annealed Co implanted in Si NTs.

ethanol EtOH, toluene, zinc nitrate hexahydrate $\rm Zn(NO_3)_2\cdot 6H_2O$, hexamethylenetetramine HMTA, from Praxair: 0.5% silane $\rm SiH_4$ in helium He, UHP grade.

Characterization was done with scanning electron microscopy (FEI Quanta 200) with energy-dispersive X-ray (EDX), Transmission electron microscopy (TEM) JEOL JEM-2100, Raman RENISHAW with an excita-

tion of 532 nm, and X-ray photoelectron spectroscopy (XPS) PHI 5000 Versaprobe Scanning XPS/UPS microscope. During the XPS measurement, Al monochromatic X-ray radiation (1486.7 eV) was focused to a spot size of about 200 μm^{2} , and the pressure of the target chamber was maintained at 9 \times 10 $^{-9}$ mbar. The spectrum was referenced using O

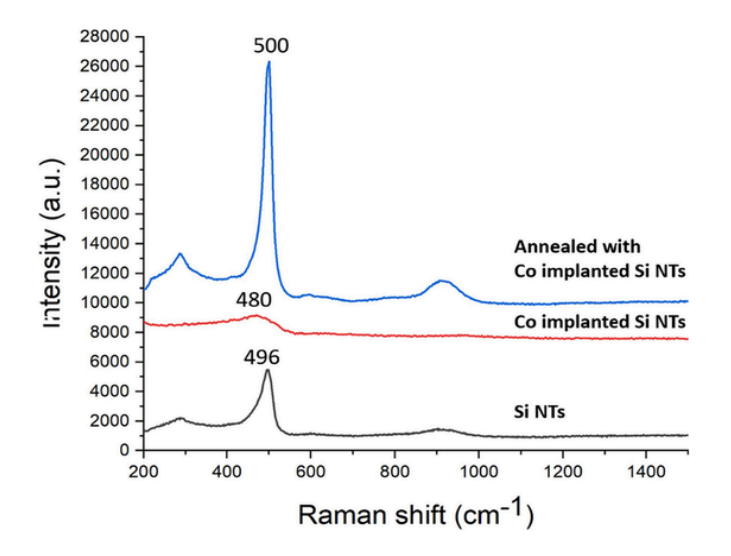


Fig. 4. Raman spectra of the as-prepared Si NTs and the Co implanted Si NTs before and after annealing.

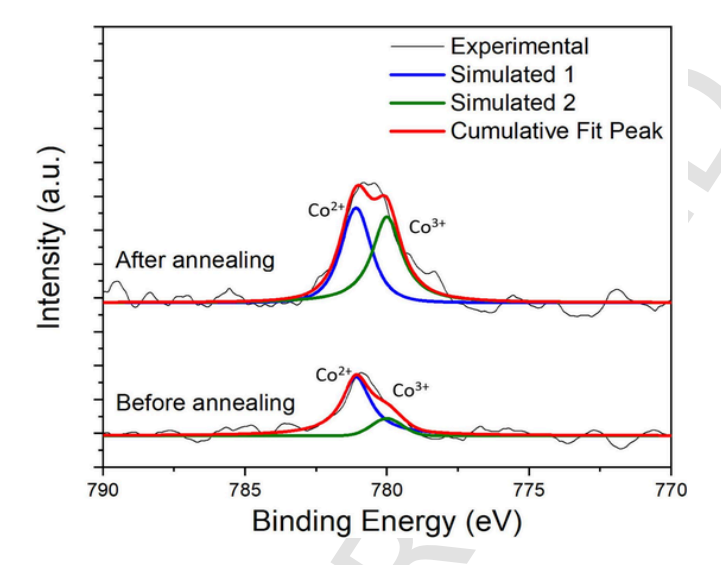


Fig. 5. High-resolution XPS of Co 2p for Co implanted Si NTs before and after annealing.

 $1~\mbox{s}$ from the native $\mbox{SiO}_2,$ and the baseline was taken using the Shirley function.

4.2. Fabrication of silicon nanotubes

ZnO nanocrystals (seeds) were prepared by mixing a solution of $\rm Zn(CH_3COO)_2$ (12.5 mL, 0.01 M), MeOH (25 mL), and NaOH (6 mL, 0.03 M) for 2 h at 60 °C. ZnO seeds were deposited on a Silicon wafer with a spin coating at 3000 rpm; then, the substrates were annealed at 300 °C for 1 h. This ZnO nanocrystal has a diameter in the range of 1–5 nm and is highly crystalline, as shown in the TEM in S1. Si wafer coated with ZnO seeds were incubated in a solution containing 0.1 M of $\rm Zn(NO_3)_2$ and 0.1 M of HTMA for 3 h at 95 °C. Silicon was deposited by a CVD process using silane as silicon precursor (0.5% SiH₄ in He) (20 sccm) diluted further in pure (UHP) He gas (250 sccm) at 540 °C for 5 min. The ZnO nanowire core was removed with 1% HCl at room temperature, followed by DI water rinsing several times.

4.3. Implantation of Cobalt ions into porous silicon nanotubes

The cobalt ion implantation was carried out using 50 keV Co- ion beam into Si NT array with a fluence of 7.5×10^{15} ions/cm² using a low energy ion implantation system available at the Ion Beam Laboratory (IBL) of the University of North Texas (UNT) [34]. A National Electrostatics Corporation (NEC) Source of negative ions by cesium sputtering (SNICS-II) was used to produce and accelerate the Co- ions from a solid cathode. In order to avoid ion channeling, the Si NT was tilted by 20 degrees to the direction of the incident beam. The implantation chamber was kept under a high vacuum with a pressure of 7.5×10^{-8} mbar. Before the implantation of the cobalt ions, the energy and fluence were estimated by a well-known ion-solid interaction simulation code SRIM [35] The simulated cobalt ion implantation concentration depth profile in silicon is shown in Fig. S6. The simulation was performed for 100,000 ions in full cascade method, including the surface sputtering effects. The silicon's density was 4.98 \times 10^{22} atoms/cm³.

CRediT authorship contribution statement

Roberto Gonzalez-Rodriguez: Writing – review & editing, Writing – original draft, Visualization, Validation, Project administration, Methodology, Investigation, Formal analysis, Data curation, Conceptualization. Bibhudutta Rout: Writing – review & editing, Writing – original draft, Resources, Methodology, Investigation, Formal analysis, Data curation. Satyabrata Singh: Methodology, Investigation. Diana Berman: Writing – review & editing, Writing – original draft, Resources, Methodology, Investigation, Formal analysis, Data curation. Evan Hathaway: Writing – review & editing,

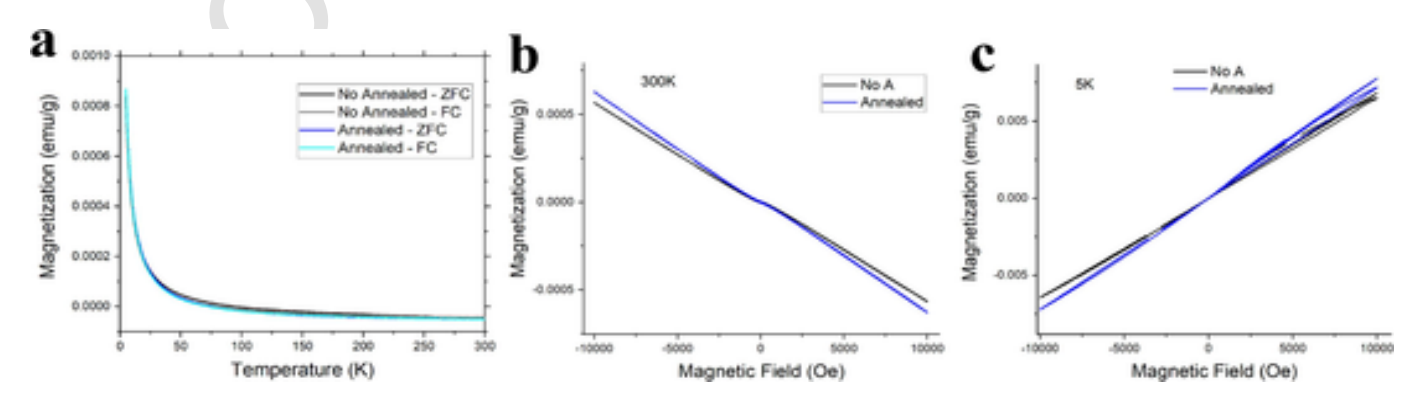


Fig. 6. a) ZFC and FC magnetization curves for Cobalt in Si NTs, magnetization curves at b) 300 K and c) 5 K.

Writing – original draft, Methodology, Investigation, Formal analysis, Data curation. Jeffery L. Coffer: Writing – review & editing, Writing – original draft, Resources, Methodology, Investigation, Formal analysis, Data curation. Yuankun Lin: Writing – review & editing, Writing – original draft, Resources, Methodology, Investigation, Formal analysis, Data curation. Jingbiao Cui: Writing – review & editing, Writing – original draft, Visualization, Validation, Supervision, Resources, Project administration, Methodology, Investigation, Funding acquisition, Formal analysis, Data curation, Conceptualization.

Declaration of competing interest

The authors declare that they have no known competing financial interests or personal relationships that could have appeared to influence the work reported in this paper.

Data availability

Data will be made available on request.

Acknowledgments

This work was supported by the U.S. National Science Foundation (#2128367).

Appendix A. Supplementary data

Supplementary data to this article can be found online at https://doi.org/10.1016/j.matchar.2024.113850.

References

- X. Zhang, et al., Stable high-capacity and high-rate silicon-based lithium battery anodes upon two-dimensional covalent encapsulation, Nat. Commun. 11 (2020) 3826, https://doi.org/10.1038/s41467-020-17686-4.
- [2] F. Priolo, T. Gregorkiewicz, M. Galli, T.F. Krauss, Silicon nanostructures for photonics and photovoltaics, Nat. Nanotechnol. 9 (2014) 19–32, https://doi.org/ 10.1038/nnano.2013.271.
- [3] A. Venuta, J. Wolfram, H. Shen, M. Ferrari, Post-nano strategies for drug delivery: multistage porous silicon microvectors, J. Mater. Chem. B 5 (2017) 207–219, https://doi.org/10.1039/C6TB01978A.
- [4] R. Gonzalez-Rodriguez, P. Granitzer, K. Rumpf, J.L. Coffer, New MRI contrast agents based on silicon nanotubes loaded with superparamagnetic iron oxide nanoparticles, R. Soc. Open Sci. 5 (2024) 180697, https://doi.org/10.1098/ rsos 180697
- [5] D. Lim, M. Kim, Y. Kim, S. Kim, Memory characteristics of silicon nanowire transistors generated by weak impact ionization, Sci. Rep. 7 (2017) 12436, https:// doi.org/10.1038/s41598-017-12347-x.
- [6] A. Sambugaro, et al., Porous silicon microparticles are efficient carriers for immunologic adjuvants, J. Drug Deliv. Sci. Technol. 92 (2024) 105301, https:// doi.org/10.1016/j.jddst.2023.105301.
- [7] D. Ge, et al., Silver Nano-dendrite-plated porous silicon substrates formed by single-step electrochemical synthesis for surface-enhanced Raman scattering, ACS Appl. Nano Mater. 3 (2020) 3011–3018, https://doi.org/10.1021/ acsanm.0c00296.
- [8] B.A. Timerkaev, et al., Electric arc synthesis of silicon nanostructures, J. Phys. Conf. Ser. 2270 (2022) 012048, https://doi.org/10.1088/1742-6596/2270/1/012048.
- [9] B.A. Timerkaev, B.R. Shakirov, D.B. Timerkaeva, Creation of silicon nanostructures in electric arc discharge, High Energy Chem. 53 (2019) 162–166, https://doi.org/10.1134/S0018143919020152.
- [10] B. Chen, et al., Branched silicon nanotubes and metal nanowires via AAO-template-assistant approach, Adv. Funct. Mater. 20 (2010) 3791–3796, https://doi.org/10.1002/adfm.201001190.
- [11] Y. Yu, A. Mendoza-Garcia, B. Ning, S. Sun, Cobalt-substituted magnetite nanoparticles and their assembly into Ferrimagnetic nanoparticle arrays, Adv. Mater. 25 (2013) 3090–3094, https://doi.org/10.1002/adma.201300595.

- [12] S. Iravani, R.S. Varma, Sustainable synthesis of cobalt and cobalt oxide nanoparticles and their catalytic and biomedical applications, Green Chem. 22 (2020) 2643–2661, https://doi.org/10.1039/D0GC00885K.
- [13] Y.A. Syed Khadar, A. Balamurugan, V.P. Devarajan, R. Subramanian, S. Dinesh Kumar, Synthesis, characterization and antibacterial activity of cobalt doped cerium oxide (CeO2:Co) nanoparticles by using hydrothermal method, J. Mater. Res. Technol. 8 (2019) 267–274, https://doi.org/10.1016/j.jmrt.2017.12.005.
- [14] J. Yang, et al., Porous carbon with uniformly distributed cobalt nanoparticles derived from ZIF-67 for efficient removal of vapor elemental mercury: A combined experimental and DFT study, Chem. Eng. J. 428 (2022) 132095, https://doi.org/ 10.1016/j.cej.2021.132095.
- [15] S.S. Kalyan Kamal, et al., Synthesis of cobalt nanoparticles by a modified polyol process using cobalt hydrazine complex, J. Alloys Compd. 474 (2009) 214–218, https://doi.org/10.1016/j.jallcom.2008.06.160.
- [16] R. Ferré, K. Ounadjela, J. George, Magnetization processes in nickel and cobalt electrodeposited nanowires, Phys. Rev. B - Condens. Matt. Mater. Phys. 56 (1997) 14066–14075, https://doi.org/10.1103/PhysRevB.56.14066.
- [17] M.-S. Wu, B. Xu, C.-Y. Ouyang, Manipulation of spin-flip in Co3O4: a first principles study, J. Mater. Sci. 51 (2016) 4691–4696, https://doi.org/10.1007/ s10853-016-9786-x.
- [18] L. Bai, et al., Charge transfer in spinel Co3O4 at high pressures, J. Phys. Condens. Matter 24 (2012) 435401, https://doi.org/10.1088/0953-8984/24/43/435401.
- [19] A. Diallo, A.C. Beye, T.B. Doyle, E. Park, M. Maaza, Green synthesis of Co3O4 nanoparticles via Aspalathus linearis: physical properties, Green Chem. Lett. Rev. 8 (2015) 30–36, https://doi.org/10.1080/17518253.2015.1082646.
- [20] K.J. Kormondy, et al., Epitaxy of polar semiconductor Co3O4 (110): growth, structure, and characterization, J. Appl. Phys. 115 (2014) 243708, https://doi.org/ 10.1063/1.4885048.
- [21] S. Singh, B. Rout, Simulation study of surface sputtering and distribution of ions in silicon due to low-energy high-fluence cobalt irradiation, Surf. Interf. 24 (2021) 101035, https://doi.org/10.1016/j.surfin.2021.101035.
- [22] X. Huang, R. Gonzalez-Rodriguez, R. Rich, Z. Gryczynski, J.L. Coffer, Fabrication and size dependent properties of porous silicon nanotube arrays, Chem. Commun. 49 (2013) 5760–5762, https://doi.org/10.1039/C3CC41913D.
- [23] R. Gonzalez-Rodriguez, N. Arad-Vosk, N. Rozenfeld, A. Sa'ar, J.L. Coffer, Control of CH3NH39bl3 perovskite nanostructure formation through the use of silicon nanotube templates, Small 12 (2016) 4477–4480, https://doi.org/10.1002/ smll.201601291.
- [24] R. Gonzalez-Rodriguez, N. Arad-Vosk, A. Sa'ar, J.L. Coffer, Phase control in mixed halide Methylammonium Lead perovskites using silicon nanotube templates, J. Phys. Chem. C 122 (2018) 20040–20045, https://doi.org/10.1021/ acs.jpcc.8b06824.
- [25] P.K. Giri, V. Raineri, G. Franzo, E. Rimini, Mechanism of swelling in low-energy ion-irradiated silicon, Phys. Rev. B 65 (2001) 012110, https://doi.org/10.1103/ PhysRevB 65 012110
- [26] R. Callec, A. Poudoulec, Characteristics of implantation-induced damage in GaSb, J. Appl. Phys. 73 (1993) 4831–4835, https://doi.org/10.1063/1.354090.
- [27] M. Kaur, S. Gautam, N. Goyal, Ion-implantation and photovoltaics efficiency: A review, Mater. Lett. 309 (2022) 131356, https://doi.org/10.1016/ i.matlet.2021.131356.
- [28] D. Negi, et al., Cobalt ion implantation assisted modifications in luminescence, surface states, structural and morphological properties of MgTiO3 thin films, Appl. Phys. A 129 (2023) 389, https://doi.org/10.1007/s00339-023-06653-7.
- [29] W. Huang, et al., Dynamic structure and chemistry of the silicon solid-electrolyte interphase visualized by cryogenic Electron microscopy, Matter 1 (2019) 1232–1245, https://doi.org/10.1016/j.matt.2019.09.020.
- [30] R. Dehghan, et al., In-situ reduction of promoted cobalt oxide supported on alumina by environmental transmission Electron microscopy, Catal. Lett. 141 (2011) 754, https://doi.org/10.1007/s10562-011-0600-8.
- [31] C. Alex, S.C. Sarma, S.C. Peter, N.S. John, Competing effect of Co3+ reducibility and oxygen-deficient defects toward high oxygen evolution activity in Co3O4 Systems in Alkaline Medium, ACS Appl. Energy Mater. 3 (2020) 5439–5447, https://doi.org/10.1021/acsaem.0c00297.
- [32] L. Liu, et al., Probing the crystal plane effect of Co3O4 for enhanced Electrocatalytic performance toward efficient overall water splitting, ACS Appl. Mater. Interfaces 9 (2017) 27736–27744, https://doi.org/10.1021/ acsami 7b07793
- [33] M. Naushad, et al., Nitrogen-doped carbon quantum dots (N-CQDs)/Co3O4 nanocomposite for high performance supercapacitor, J. King Saud Univ. Sci. 33 (2021) 101252, https://doi.org/10.1016/j.jksus.2020.101252.
- [34] B. Rout, et al., An overview of the facilities, activities, and developments at the University of North Texas ion Beam Modification and analysis laboratory (IBMAL), AIP Conf. Proc. 1544 (2013) 11–18, https://doi.org/10.1063/1.4813454.
- [35] J.P. Biersack, L.G. Haggmark, A Monte Carlo computer program for the transport of energetic ions in amorphous targets, Nucl. Inst. Methods 174 (1980) 257–269, https://doi.org/10.1016/0029-554X(80)90440-1.